

An optimized surface plasmon photovoltaic structure using energy transfer between discrete nano-particles

Albert Lin,^{1,*} Sze-Ming Fu,¹ Yen-Kai Chung,² Shih-yun Lai,¹ and Chi-Wei Tseng¹

¹Department of Electronic Engineering, National Chiao-Tung University, Hsinchu 30010, Taiwan

²Department of Eelectro-Physics, National Chiao-Tung University, Hsinchu 30010, Taiwan
[*hdt5746@gmail.com](mailto:hdt5746@gmail.com)

Abstract: Surface plasmon enhancement has been proposed as a way to achieve higher absorption for thin-film photovoltaics, where surface plasmon polariton (SPP) and localized surface plasmon (LSP) are shown to provide dense near field and far field light scattering. Here it is shown that controlled far-field light scattering can be achieved using successive coupling between surface plasmonic (SP) nano-particles. Through genetic algorithm (GA) optimization, energy transfer between discrete nano-particles (ETDNP) is identified, which enhances solar cell efficiency. The optimized energy transfer structure acts like lumped-element transmission line and can properly alter the direction of photon flow. Increased in-plane component of wavevector is thus achieved and photon path length is extended. In addition, Wood-Rayleigh anomaly, at which transmission minimum occurs, is avoided through GA optimization. Optimized energy transfer structure provides 46.95% improvement over baseline planar cell. It achieves larger angular scattering capability compared to conventional surface plasmon polariton back reflector structure and index-guided structure due to SP energy transfer through mode coupling. Via SP mediated energy transfer, an alternative way to control the light flow inside thin-film is proposed, which can be more efficient than conventional index-guided mode using total internal reflection (TIR).

©2012 Optical Society of America

OCIS codes: (310.6845) Thin film devices and applications; (040.5350) Photovoltaic.

References and links

1. S. A. Maier, P. G. Kik, H. A. Atwater, S. Meltzer, E. Harel, B. E. Koel, and A. A. G. Requicha, "Local detection of electromagnetic energy transport below the diffraction limit in metal nanoparticle plasmon waveguides," *Nat. Mater.* **2**(4), 229–232 (2003).
2. J. R. Krenn, "Nanoparticle waveguides: Watching energy transfer," *Nat. Mater.* **2**(4), 210–211 (2003).
3. S. A. Maier, P. G. Kik, and H. A. Atwater, "Optical pulse propagation in metal nanoparticle chain waveguides," *Phys. Rev. B* **67**, 205402 (2003).
4. H. A. Atwater and A. Polman, "Plasmonics for improved photovoltaic devices," *Nat. Mater.* **9**(3), 205–213 (2010).
5. W. Bai, Q. Gan, F. Bartoli, J. Zhang, L. Cai, Y. Huang, and G. Song, "Design of plasmonic back structures for efficiency enhancement of thin-film amorphous Si solar cells," *Opt. Lett.* **34**(23), 3725–3727 (2009).
6. F. J. Beck, S. Mookkapati, and K. R. Catchpole, "Light trapping with plasmonic particles: beyond the dipole model," *Opt. Express* **19**(25), 25230–25241 (2011).
7. F. J. Beck, S. Mookkapati, A. Polman, and K. R. Catchpole, "Asymmetry in photocurrent enhancement by plasmonic nanoparticle arrays located on the front or on the rear of solar cells," *Appl. Phys. Lett.* **96**(3), 033113 (2010).
8. K. R. Catchpole and A. Polman, "Plasmonic solar cells," *Opt. Express* **16**(26), 21793–21800 (2008).
9. D. Cheyns, B. P. Rand, B. Verreert, J. Genoe, J. Poortmans, and P. Heremans, "The angular response of ultrathin film organic solar cells," *Appl. Phys. Lett.* **92**(24), 243310 (2008).
10. V. E. Ferry, M. A. Verschuuren, H. B. T. Li, E. Verhagen, R. J. Walters, R. E. I. Schropp, H. A. Atwater, and A. Polman, "Light trapping in ultrathin plasmonic solar cells," *Opt. Express* **18**(S2 Suppl 2), A237–A245 (2010).
11. N. Lagos, M. M. Sigalas, and E. Lidorikis, "Theory of plasmonic near-field enhanced absorption in solar cells," *Appl. Phys. Lett.* **99**(6), 063304 (2011).

12. K. Q. Le, A. Abass, B. Maes, P. Bienstman, and A. Alù, "Comparing plasmonic and dielectric gratings for absorption enhancement in thin-film organic solar cells," *Opt. Express* **20**(S1), A39–A50 (2012).
13. A. Meyer and H. Ade, "The effect of angle of incidence on the optical field distribution within thin film organic solar cells," *J. Appl. Phys.* **106**(11), 113101 (2009).
14. C. Min, J. Li, G. Veronis, J.-Y. Lee, S. Fan, and P. Peumans, "Enhancement of optical absorption in thin-film organic solar cells through the excitation of plasmonic modes in metallic gratings," *Appl. Phys. Lett.* **96**(13), 133302 (2010).
15. J. N. Munday and H. A. Atwater, "Large Integrated Absorption Enhancement in Plasmonic Solar Cells by Combining Metallic Gratings and Antireflection Coatings," *Nano Lett.* **11**(6), 2195–2201 (2011).
16. U. W. Paetzold, E. Moulin, D. Michaelis, W. Bottler, C. Wächter, V. Hagemann, M. Meier, R. Carius, and U. Rau, "Plasmonic reflection grating back contacts for microcrystalline silicon solar cells," *Appl. Phys. Lett.* **99**(18), 181105 (2011).
17. U. W. Paetzold, E. Moulin, B. E. Pieters, R. Carius, and U. Rau, "Design of nanostructured plasmonic back contacts for thin-film silicon solar cells," *Opt. Express* **19**(S6 Suppl 6), A1219–A1230 (2011).
18. W. E. I. Sha, W. C. H. Choy, and W. C. Chew, "Angular response of thin-film organic solar cells with periodic metal back nanostrips," *Opt. Lett.* **36**(4), 478–480 (2011).
19. H.-Y. Lin, Y. Kuo, C.-Y. Liao, C. C. Yang, and Y.-W. Kiang, "Surface plasmon effects in the absorption enhancements of amorphous silicon solar cells with periodical metal nanowall and nanopillar structures," *Opt. Express* **20**(S1), A104–A118 (2012).
20. S. Pillai, F. J. Beck, K. R. Catchpole, Z. Ouyang, and M. A. Green, "The effect of dielectric spacer thickness on surface plasmon enhanced solar cells for front and rear side depositions," *J. Appl. Phys.* **109**(7), 073105 (2011).
21. Y.-W. Jiang, L. D.-C. Tzuang, Y.-H. Ye, Y.-T. Wu, M.-W. Tsai, C.-Y. Chen, and S.-C. Lee, "Effect of Wood's anomalies on the profile of extraordinary transmission spectra through metal periodic arrays of rectangular subwavelength holes with different aspect ratio," *Opt. Express* **17**(4), 2631–2637 (2009).
22. V. Shah, H. Schade, M. Vanecek, J. Meier, E. Vallat-Sauvain, N. Wyrsh, U. Kroll, C. Droz, and J. Bailat, "Thin-film silicon solar cell technology," *Prog. Photovolt. Res. Appl.* **12**(23), 113–142 (2004).
23. J. M. Khoshman and M. E. Kordesch, "Optical constants and band edge of amorphous zinc oxide thin films," *Thin Solid Films* **515**(18), 7393–7399 (2007).
24. S. J. Kang and Y. H. Joung, "Influence of substrate temperature on the optical and piezoelectric properties of ZnO thin films deposited by rf magnetron sputtering," *Appl. Surf. Sci.* **253**(17), 7330–7335 (2007).
25. C. Munuera, J. Zuniga-Perez, J. F. Rommeluere, V. Sallet, R. Triboulet, F. Soria, V. Munoz-Sanjose, and C. Ocal, "Morphology of ZnO grown by MOCVD on sapphire substrates," *J. Cryst. Growth* **264**(1-3), 70–78 (2004).
26. A. S. Ferlauto, G. M. Ferreira, J. M. Pearce, C. R. Wronski, R. W. Collins, X. Deng, and G. Ganguly, "Analytical model for the optical functions of amorphous semiconductors and its applications for thin film solar cells," *Thin Solid Films* **455–456**, 388–392 (2004).
27. H. Kim, A. Pique, J. S. Horwitz, H. Murata, Z. H. Kafafi, C. M. Gilmore, and D. B. Chrisey, "Effect of aluminum doping on zinc oxide thin films grown by pulsed laser deposition for organic light-emitting devices," *Thin Solid Films* **377–378**, 798–802 (2000).
28. E. D. Palik, *Handbook of optical constants of solids* (Academic Press, 1985).
29. A. Lin and J. D. Phillips, "Optimization of random diffraction gratings in thin-film solar cells using genetic algorithms," *Sol. Energy Mater. Sol. Cells* **92**(12), 1689–1696 (2008).
30. P. Bhattacharya, *Semiconductor optoelectronic devices, 2nd ed.* (Prentice-Hall, 2006).
31. C. AB, *Comsol multiphysics RF module user guide V 3.3* (2006).
32. Synopsys, "Sentaurus device EMW user manual V. X-2005.10," (2005), pp. 78–79.
33. G. V. Naik, J. L. Schroeder, X. Ni, A. V. Kildishev, T. D. Sands, and A. Boltasseva, "Titanium nitride as a plasmonic material for visible and near-infrared wavelengths," *Opt. Mater. Express* **2**(4), 478–489 (2012).
34. M. Y. Kuo, J. Y. Hsing, T. T. Chiu, C. N. Li, W. T. Kuo, T. S. Lay, and M. H. Shih, "Quantum efficiency enhancement in selectively transparent silicon thin film solar cells by distributed Bragg reflectors," *Opt. Express* **20**(S6 Suppl 6), A828–A835 (2012).
35. B. P. Rand, P. Peumans, and S. R. Forrest, "Long-range absorption enhancement in organic tandem thin-film solar cells containing silver nanoclusters," *J. Appl. Phys.* **96**(12), 7519–7526 (2004).

1. Introduction

Energy transfer is a peculiar phenomenon existing in surface plasmon nano-particles [1–3], where efficient electromagnetic power is coupled through successive metal particles. There has been tremendous amount on application of surface plasmon to photovoltaic cells as an emerging technique to extend photon path length. SPP & LSP have been demonstrated to enhance the light absorption by wide angle scattering by SP and strongly localized field intensity at metallic/semiconductor interface [4–20]. In this paper, surface plasmon mediated energy transfer phenomenon is further tailored to increase solar cell absorbance using global optimization methods, resulting in coupling between top/bottom and adjacent metallic nano-particles which corresponds to vertical and lateral energy transfer. In addition, the Wood-Rayleigh anomaly where transmittance minimum exists is avoided [21]. Compared to

conventional optical waveguiding with index-guided(IG) mode [22] where total internal reflection (TIR) is used to successively reflect photons back into semiconductor film, surface plasmon (SP) energy transfer(ET) provides larger scattering angle and larger in-plane wavevector component inside device cavity. As a result of genetic algorithm optimization, energy transfer between top/Bottom and adjacent nano-particles is observed. In this scenario, Ag nano-particle array essentially acts like a lumped-element transmission line, and it efficiently alters/guides the direction of photon flux flow. The in-plane component of photon wavevector is increased inside the semiconductor film, and higher absorbance is thus achieved due to the phenomenon of surface plasmonic energy transfer between discrete nano-particles (ETDNP).

2. Principle of surface plasmon mediated energy transfer

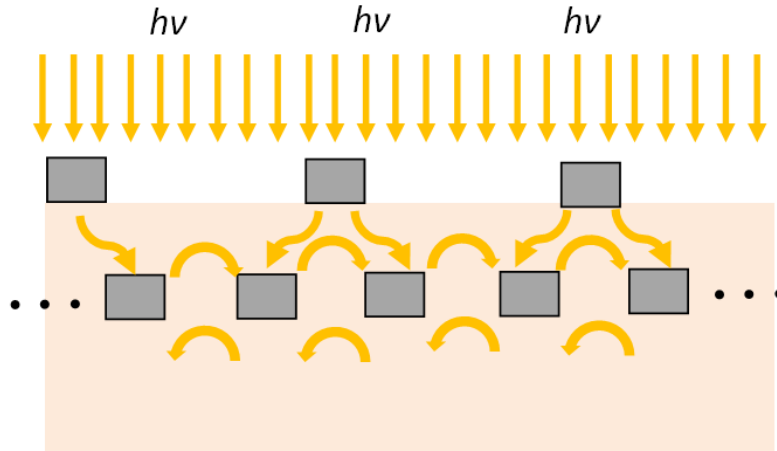


Fig. 1. Illustration of SP mode coupling between discrete metallic nano-particles.

Energy transfer (ET) between metallic nano-particle has been employed to realize optical waveguide [1–3]. In contrast to conventional index-guided mode utilizing total internal reflection (TIR), Energy transfer (ET) mediated by surface plasmon uses coupling between nano-particles to achieve waveguiding effect. This is essentially lumped-element transmission line. Since SP can condense the light below diffraction limit, the phenomenon can possibly be utilized to enhance solar cell light trapping and optical confinement to the extent that is not achievable by only index guiding. Figure 1 illustrates the principles of surface plasmon energy transfer. The energy transfer structure under study is no back reflector to isolate the effect of SP mediated energy transfer.

Material parameters can be referenced in literature [23–27]. Silver refractive index and extinction coefficient is from Palik [28]. Silicon refractive index and extinction coefficient is from SOPRA. The calculation of pointing vector and absorption loss follows:

$$\begin{aligned} \vec{P}_{\text{poynting}} &= \vec{E}(\vec{r}) \times \vec{H}(\vec{r}) \\ P_{\text{absorption}} &= \vec{E}(\vec{r}) \cdot \vec{J}(\vec{r}) = \vec{E}(\vec{r}) \cdot \sigma(\lambda) \vec{E}(\vec{r}) \end{aligned} \quad (1)$$

where E and H is electric and magnetic field, J is current density induced by electromagnetic radiation and σ is conductivity which is related to the imaginary part of complex permittivity and characterizes material absorption property. Poynting vector characterizes the incident power per unit area and absorption power is in unit of energy per second per unit volume. Notice absorption power has to be divided by photon energy to be converted to photocurrent generation since one photon generates one electron-hole pair, unless novel third-generation schemes such as low threshold Auger or intermediate band solar cell can be realized. The

procedure for solving Helmholtz equation, calculating spectral response and integrated absorbance can be found in literature [29–32]. In this work, the discretization of Maxwell's equation is carried out by two-dimensional finite element method, using COMSOL Multiphysics software package [31]. The incident light illumination on solar cell is TM polarized plane wave with wavelengths in the range of 400 nm-1000 nm, which is the wavelength range of interest for silicon material. Only TM polarized wave is of interest since TE wave does not lead to surface plasmonic effect in two dimensional problems [12]. Periodic boundary conditions are set at the left and right boundaries, while perfectly matched layer absorbing boundary conditions are used at the top and bottom boundaries of the computational domain. The absorbance in silicon is then calculated by integrating the divergence of the time-averaged Poynting vector, which is then normalized by incident power. Only absorbance in silicon generates electron-hole while absorbance in metal leads to surface plasmon absorption loss.

3. Evolutionary structures for energy transfer

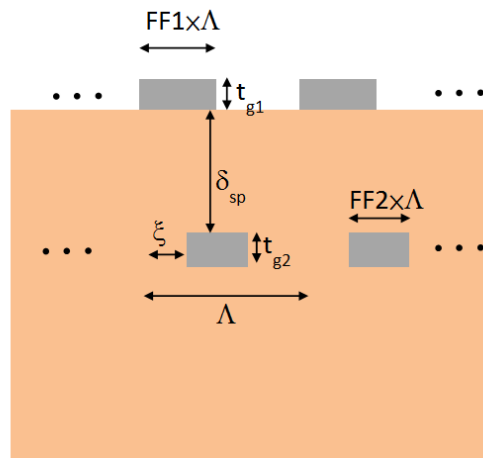


Fig. 2. The first attempt of SP energy transfer structure and its parameters to be optimized.

The first evolutionary structure consists of a dual SP grating on top and in the middle of silicon thin film, as illustrated in Fig. 2. The coupling of re-emitted photons by Ag nanoparticles is expected to further increase absorbance, compared to simple far-field enhancement. Geometrical optimization is done by adjusting each dimension, including the nano-particle heights t_{g1} and t_{g2} , the fill factor of both grating FF_1 and FF_2 , the separation between top and middle nano-particle arrays δ_{sp} , the mis-alignment between two nano-particle array ξ , and period Λ . The coupling of SP mode between top and bottom Ag arrays and coupling between adjacent Ag nano-particle is the phenomenon that is expected to enhance photon harvesting.

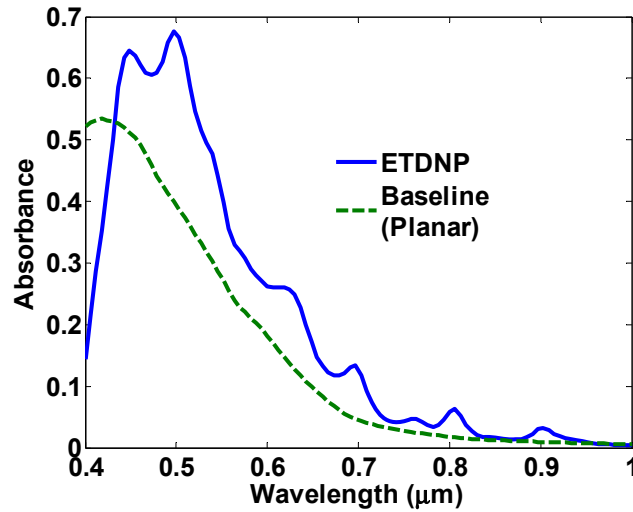


Fig. 3. Spectral response for initial attempt of optimized SP energy transfer structure.

After GA optimization, $t_{g1} = 0.0759\mu\text{m}$ and $t_{g2} = 0.0497\mu\text{m}$, the fill factor of both grating $FF_1 = 0.4419$ and $FF_2 = 0.3$, the separation between top and middle nano-particle arrays $\delta_{sp} = 0.2\mu\text{m}$, the mis-alignment between two nano-particle array $\xi = 0.081\mu\text{m}$, period $\Lambda = 0.25\mu\text{m}$, and silicon thickness is kept $0.3\mu\text{m}$ throughout evolution. The spectral response for the first evolutionary structure is shown in Fig. 3. The baseline is planar silicon slab cell without any Ag particle on either top surface or inside silicon thin film. The short wavelength absorbance peaks for ETDNP at $\lambda = 448.5\text{nm}$ and 497nm in the spectral response are likely due to Fabry-Perot type of quasi-guided mode excitation. In current structure there is no back reflector and thus the thin film absorbance is greatly affected by transmission through front surface. Since it is observed that there is not any absorbance dip in spectral response, it is evident that wood-Rayleigh anomaly [21] is avoided as a result of GA optimization. The integrated optical absorbance, without back reflector, in the first evolutionary structure is 20.46%. Further improvement can be attained by enhancing the lateral power flow via stronger coupling into Bloch in-plane propagation mode, to increase power absorption. This can be done by using a more sophisticated evolutionary structure where inside silicon film there are two more closely spaced Ag nano-particles per period.

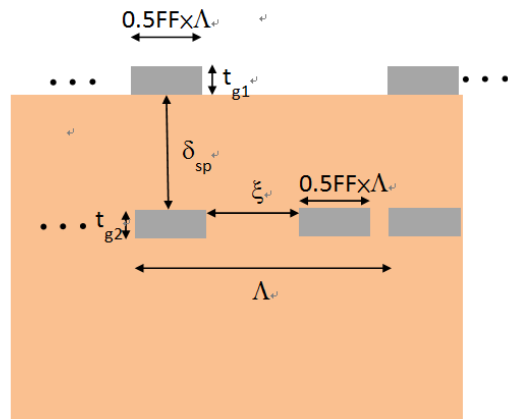


Fig. 4. The second SP energy transfer structure and its parameters to be optimized.

The second evolutionary structure also consists of a dual surface plasmon grating at the top and in the middle of silicon thin film, as illustrated in Fig. 4. The difference, compared to the first evolutionary structure, is that the bottom Ag array is now with two Ag particles per period and these two Ag particles can freely move in the lateral direction during optimization. The coupling of re-emitted photon by Ag nano-particles is expected to be enhanced, especially between adjacent Ag particles, which in turn can increase in-plane propagation of solar photons and thus optical guiding and confinement. Geometrical optimization is done by adjusting each dimension, including the nano-particle heights t_{g1} and t_{g2} , the fill factor FF, the separation between both nano-particle arrays δ_{sp} , the separation between two adjacent nano-particles in the bottom Ag array ξ , and period Λ . The second evolutionary structure possesses more complicated geometrical parameterization but will lead to more design flexibility. The geometry after optimization is $\Lambda = 0.3698\mu\text{m}$, $\delta_{sp} = 0.2\mu\text{m}$, $t_{g1} = 0.0813\mu\text{m}$, $t_{g2} = 0.05\mu\text{m}$, $\text{FF} = 0.4$, $\xi = 0.1095\mu\text{m}$, and silicon film thickness is also kept $0.3\mu\text{m}$.

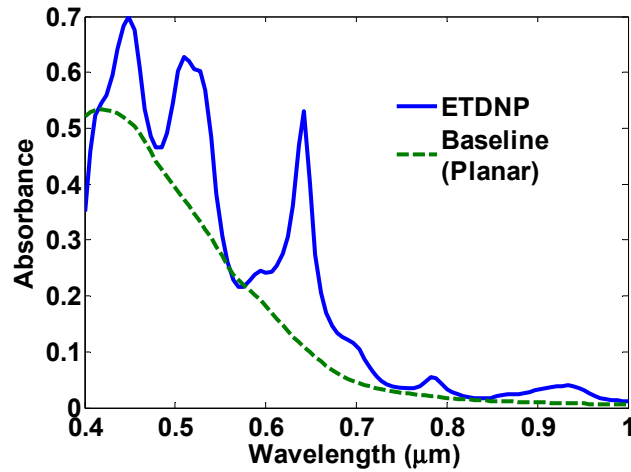


Fig. 5. Spectral response for the Optimized second evolutionary structure with more closely spaced bottom Ag grating

Figure 5 is the spectral response for the second evolutionary structure with modified, more closely spaced Ag particles inside silicon film. The baseline is planar silicon slab cell without any Ag particle on either top surface or inside silicon thin film. The peak for ETDNP at $\lambda = 448.5\text{nm}$ and $\lambda = 509.1\text{nm}$ is due to Fabry-Perot like quasi-guided mode. The peak at $\lambda = 642.4\text{nm}$ is likely due to the initiation of energy transfer between Ag nano-particles which will be more evident if looking at field profile plot in the following paragraph (Fig. 7 & Fig. 8). In this scenario the Ag nano-particles essentially act as SP waveguide and power is efficiently coupled between top/bottom Ag array and adjacent Ag particles. Wood-Rayleigh anomaly is again avoided by GA [21]. The integrated optical absorbance of optimized structure is 21.47%, compared to 20.46% for optimized first evolutionary structure, and 15.58% for optimal baseline cell. In contrast to conventional index-guided mode where TIR is used to achieve waveguiding, energy transfer using mode coupling between Ag particles can potentially achieve higher light trapping capability, due to the surface plasmon propagation, field condensation, photon re-emission, far field light scattering and coupling to adjacent nano-particles, and combined mechanism of these. For index guided mode, diffraction is primarily the underlying phenomenon for light trapping while surface plasmon effect is the beyond-diffraction-limit phenomenon.

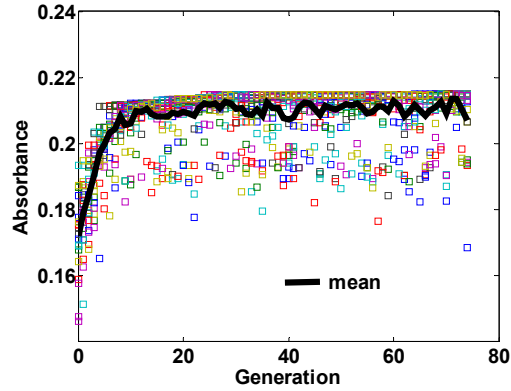


Fig. 6. Genetic algorithm statistics for the second evolutionary structure.

Figure 6 shows the details of GA evolution. The values of integrated optical absorbance within a generation are plotted as scattered points and the mean within one generation is shown in thick black line. It is observed that there is initial increase in absorbance and saturation after enough number of generations. This is typical GA running procedure. In this study, 20 individuals are employed in each generation, the generation gap is 0.9, and the recombination rate is 0.7. Compared the non-optimized population mean at generation 0 to the mean at saturation, there is 22% increase in absorbance, demonstrating the effectiveness of GA for locating integrated absorbance maximal.

4. Launching of surface plasmon mode

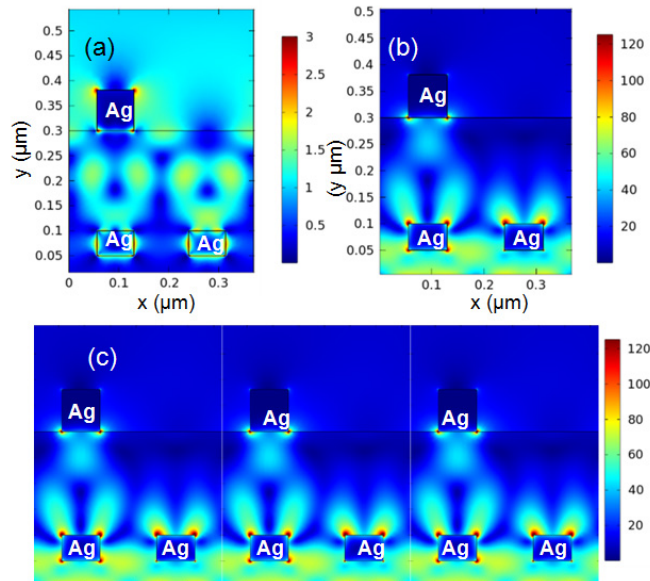


Fig. 7. Electric field profile of optimized energy transfer structure at $\lambda = 642.4\text{nm}$ (a) for scattering problem (b) for corresponding eigen mode (c) successive mode coupling between adjacent nano-particles.

Figure 7 is the field profile at $\lambda = 642.4\text{nm}$ and corresponding eigen mode profile. It is obvious that the similarity between two field profiles is the direct evidence of eigen mode excitation. The photon re-emission from metallic Ag particle is pronounced since in the field profiles for both scattering and eigen mode problems, strong upward field emission especially

from middle Ag grating inside silicon thin-film is observed. The field intensity is strong at bottom Ag particle, as is evident from Fig. 7(a). This is the result of coupling of SP mode between adjacent Ag particles, which enhances the lateral power flow and in-plane wave propagation. Photon life time and light trapping can therefore be promoted. Localized surface plasmon (LSP) is observed especially at corner of Ag, though the effect is not very pronounced. The LSP might subject to carrier interface recombination. Surface plasmon polariton(SPP) is not observed since no metallic back reflector exist and no evanescent wave can propagate along metal dielectric interface.

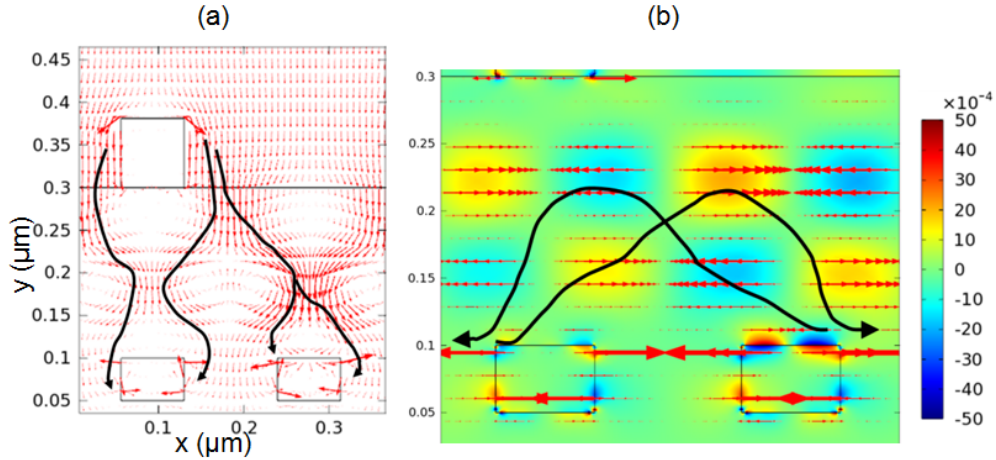


Fig. 8. (a) Vector field plot of Poynting vector for optimized energy transfer structure at $\lambda = 642.4\text{nm}$. (b) lateral component of Poynting vector at $\lambda = 642.4\text{nm}$.

Figure 8(a) plots the time-averaged Poynting vector in SP solar cell. It is observed that the coupling between top/ bottom metallic particle is very pronounced. It should be pointed out that since this is the field profile of vertical scattering problem, the direction of power flow is still primarily in negative y direction as is evident from Fig. 8(a). Therefore, the vertical coupling between adjacent Ag particles is easier to observe, while the lateral coupling between nano-particles is blurred by the strong field profile of incident wave. In order to observe the lateral coupling, the x-component of Poynting vector P_x is plotted in Fig. 8(b):

$$\begin{aligned} \bar{P}_{\text{poynting, avg}} &= P_{\text{poynting, avg, x}} \hat{a}_x + P_{\text{poynting, avg, y}} \hat{a}_y \\ &= \frac{1}{2} \text{Re} \{ E_y(\vec{r}) * H_z^*(\vec{r}) \} \hat{a}_x - \frac{1}{2} \text{Re} \{ E_x(\vec{r}) * H_z^*(\vec{r}) \} \hat{a}_y \end{aligned} \quad (2)$$

From Fig. 8(b) it can be seen there exists field pattern with two types of alternating localized field spots, i.e. blue and orange in the profile of Fig. 8(b). The direction of P_x in these two spots are in reversed direction and consecutive lateral power flow can be identified by the black arrows as drawn. The lateral power transfer starts from the surface of Ag particle and then it will go through successive blue (or orange) spots, and then settles at the surface of adjacent Ag particles. This type of energy transfer using SP metal particle as lumped-element transmission line is the phenomenon utilized here to increase light-trapping in thin-film photovoltaics due to its capability to increase in-plane propagation, therefore resulting in large scattering angle and extended photon path length.

5. Angular distribution of plasmon dipole emission

It is illustrative to study the angular characteristic of proposed Energy Transfer between Discrete Nano-Particle (ETDNP) enhancement, and compare it to widely studied surface

plasmon polariton(SPP) enhancement and conventional index-guided (IG) enhancement. At steady state the time-averaged electromagnetic energy store in a finite volume is constant:

$$\frac{\partial E_{\text{EMW,avg}}}{\partial t} = 0 \quad (3)$$

Therefore, the Poynting theorem can be written as:

$$\int_V P_{\text{Loss,avg}} dV + \oint_S \vec{P}_{\text{poynting,avg}} \cdot d\vec{S} = 0 \quad (4)$$

where $P_{\text{Loss,avg}}$, and $P_{\text{poynting,avg}}$ is the time-averaged power loss per unit volume and time-averaged Poynting vector in unit of watt per unit area. Notice that dV represents volume integration and dS represents surface integration. The time-average evaluation is necessary since the field is time-harmonic. Equation (4) can be expanded as:

$$\begin{aligned} & \frac{1}{2} \int_V \text{Re}\{\vec{E}(\vec{r}) \cdot \vec{J}^*(\vec{r})\} dV + \frac{1}{2} \oint_S \text{Re}\{\vec{E}(\vec{r}) \times \vec{H}^*(\vec{r})\} \cdot d\vec{S} \\ &= \frac{1}{2} \int_V \vec{E}(\vec{r}) \cdot \sigma(\lambda) \vec{E}^*(\vec{r}) dV + \frac{1}{2} \oint_S \text{Re}\{\vec{E}(\vec{r}) \times \vec{H}^*(\vec{r})\} \cdot d\vec{S} \\ &= 0 \end{aligned} \quad (5)$$

where E and H is electric and magnetic field intensity, J is electromagnetic wave induced current density, and σ is material conductivity at optical frequency. From Eq. (4) and Eq. (5), it is known that at every point on computing grid there is a Poynting vector indicating the power flow direction. For efficient waveguiding of solar photons, the power flow should be parallel to the film (perpendicular to the film growth direction) to ensure the longest optical path length. In order to characterize the angular distribution of electromagnetic wave inside silicon thin-film, the angle of Poynting vector is evaluated throughout entire silicon thin-film:

$$\theta = \tan^{-1} \frac{P_{\text{poynting, avg, x}}}{P_{\text{poynting, avg, y}}} = \tan^{-1} \frac{\text{Re}\{E_y(\vec{r}) * H_z^*(\vec{r})\}}{-\text{Re}\{E_x(\vec{r}) * H_z^*(\vec{r})\}} \quad (6)$$

The result is then plotted in polar plane, and the angular feature can thus be observed and compared. The averaged angle, θ_{avg} is calculated by first modulus the angle by 180° and then minus it by 90° . Afterward absolute value of the result is taken. Averaging over entire silicon thin-film region weighted by the magnitude of Poynting vector is performed to arrive the final answer for θ_{avg} .

$$\begin{aligned} \theta_{\text{avg}} &= \frac{\sum_{\theta=0}^{2\pi} \left| \text{modulus}(\theta, \pi) - \frac{\pi}{2} \right| \times \|\vec{P}_{\text{poynting, avg}}(\theta)\|}{\sum_{\theta=0}^{2\pi} \|\vec{P}_{\text{poynting, avg}}(\theta)\|} \\ &= \frac{\sum_{\theta=0}^{\pi} \left| \theta - \frac{\pi}{2} \right| \times \|\vec{P}_{\text{poynting, avg}}(\theta)\| + \sum_{\theta=\pi}^{2\pi} \left| \theta - \frac{3\pi}{2} \right| \times \|\vec{P}_{\text{poynting, avg}}(\theta)\|}{\sum_{\theta=0}^{2\pi} \|\vec{P}_{\text{poynting, avg}}(\theta)\|} \end{aligned} \quad (7)$$

The averaged angle, θ_{avg} , is used to evaluate the deviation of power flow from the in-plane Bloch wavevector direction, which is x-direction in our simulation. The second line in Eq. (7) better reflects this point. The second line of Eq. (7) can be derived from the first line of Eq. (7) by simple algebraic manipulation. The justification for using Eq. (7) to calculate θ_{avg} is that from the viewpoint of deviation from in-plane parallel Bloch wavevector direction(x-axis), there is mirror symmetry about both x- and y-axis since the deviation from Bloch wavevector direction(x-axis) is the same for $90^\circ + \theta$ and $90^\circ - \theta$, or $180^\circ + \theta$ and $180^\circ - \theta$. The

Bloch wavevector is the direction where waveguiding effect is most significant since photons propagate in parallel to the film. From the viewpoint of escape cone, symmetry about y-axis also exists where $90^\circ + \theta = 90^\circ - \theta$, since critical angle is no left-incidence or right-incidence preference. In addition, there is also mirror symmetry about x-axis where $180^\circ + \theta = 180^\circ - \theta$, due to the fact that large angle downward power flow is likely to result in large angle upward power flow. This is true because for the case of planar back reflector this certainly holds because incident angle equals reflection angle. For the case of corrugated back reflector, this is also a reasonable assumption since scattering component is strongest in its specular direction. That is the reason that in all cases large angle light scattering is desirable.

The angular distribution of Poynting vector is very crucial for thin-film solar cell since it determines the effectiveness of total internal reflection(TIR) and photon path length inside the film. The stronger the coupling of incident power into Bloch in-plane propagation mode is, the more efficient the light trapping can be achieved. If all of the incident wave power is coupled into the in-plane propagation mode, the film-thin solar cell is essentially acting as perfect waveguide. Mathematically, this concept is expressed as Bloch theorem:

$$\vec{E}(\vec{r}) = \vec{u}(\vec{r}) \exp(i\vec{k}_{\text{inPlane}} \cdot \vec{r}) \quad (8)$$

The k_{inPlane} is the in-plane component of incident wavevector. It can be seen from Eq. (8) that if efficient coupling into Bloch propagation mode is achieved, the photon actually propagates in solar cell as plane wave, until it is fully absorbed by thin-film.

From previous section, it has been shown that plasmonic nanoparticle enhances lateral in-plane wave propagation, evident from the field profile plots. This is due to the fact that photon re-emission by SP can be significantly off-normal and afterward successive coupling between adjacent plasmonic nano-particles initiates energy transfer between them. In order to see the maximal angular scattering capability, the wavelength at peak absorption in spectral response is chosen, and corresponding Poynting vector inside silicon thin-film is plotted at polar plan. To compare proposed energy transfer mode to surface plasmon polariton(SPP) mode and conventional index-guided (IG) mode, the middle Ag grating inside silicon thin-film in energy transfer structure is replaced by grated Ag back reflector or grated ZnO/Ag back reflector. The grating height, t_g in GA optimization is limited to 30nm to 50nm to be compatible with ultra-thin plasmonic solar cell. In this thin grating height range, the scattering increases with t_g . This is evident from the fact that after GA optimization, optimal t_{g2} is 50nm for ETDNP. Thus for comparison study, t_g is chosen to be 50nm. Grating period Λ is 0.3698 μm to be consistent with study in Section 3, and notice there are two gratings per period. Figure 9, Fig. 10, and Fig. 11 plots the angular distribution of Poynting vector, spectral response, and field profile for ETDNP, SPP, and IG, respectively. The Poynting vector plot and field profile is plotted at peak wavelength as indicated in the figure: $\lambda = 642.4\text{nm}$ for ETDNP, $\lambda = 812.1\text{nm}$ for SPP, and $\lambda = 606.1\text{nm}$ for IG. For ETDNP there is no back reflector at the backside of device to be consistent with the study in the previous sections. For SPP and IG there are back reflectors. The integrated absorbance is 21.47% for ETDNP, 28.59% for SPP, and 26.91% for IG. Surprisingly, the integrated absorbance of ETDNP is not significantly lower than the other two configurations, even in the absence of back reflector. This is attributed to tailored energy transfer and waveguiding effect of ETDNP mode.

5.1 Energy transfer between discrete nano-particles (ETDNP)

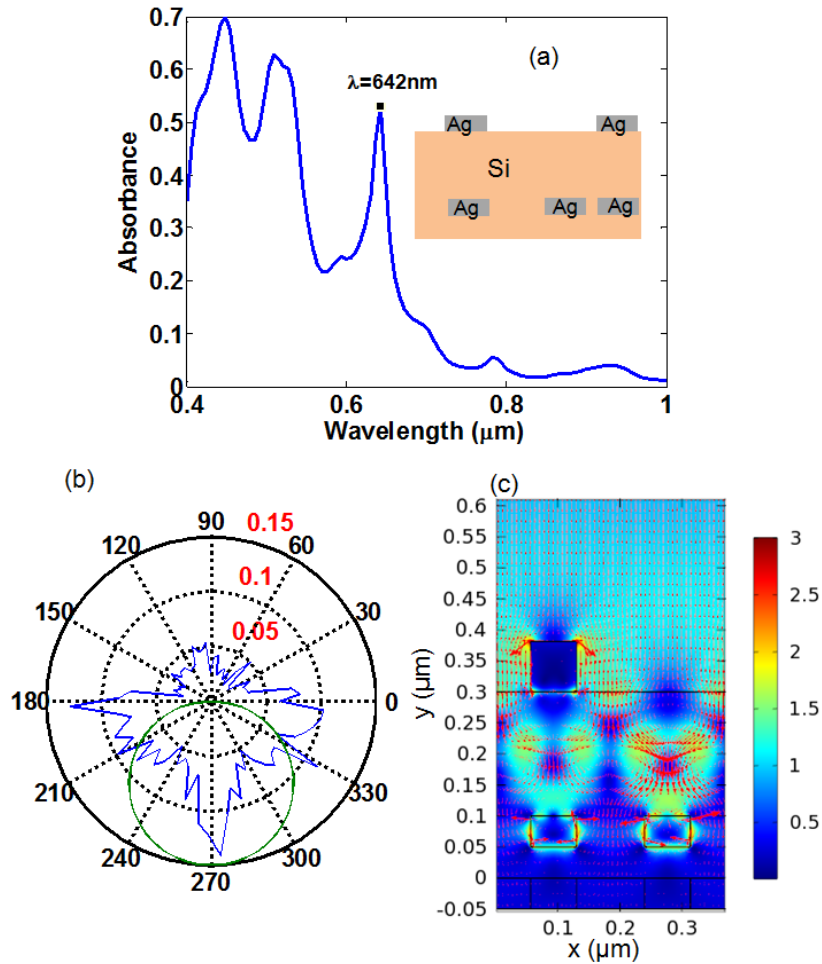


Fig. 9. (a) Spectral response, (b) angular distribution of Poynting vector, and (c) electric field profile for energy transfer between discrete nano-particles (ETDNP) at $\lambda = 642\text{nm}$.

The Red arrows in the filed profile is the Poynting vector and the field profile itself plots electric field norm. The first two peaks in the spectral response (Fig. 9(a)) are due to Fabry-Perot type resonance where standing wave between top and bottom interface is formed and absorbance enhancement is thus achieved, and the corresponding field profiles are not included for paper length consideration. In order to observe the enhancement due to energy transfer between discrete nano-particles, the third absorbance peak is chosen. The energy transfer phenomenon is more pronounced in long wavelength portion because of weak absorption. Light trapping is also the most important in this long wavelength regime of solar spectrum. From the spectral response and the angular emission plot, it is seen that wide angle emission is achieved by energy transfer between nano-particles. The angular plot shows an averaged angle of 48.29° , which is significantly higher than the averaged angle for SPP(44.42°) and IG(34.47°) enhancement at absorption peak. Therefore, large in-plane Bloch type propagation can be realized by SP nano-particle mode coupling.

5.2 Surface plasmon polariton (SPP)

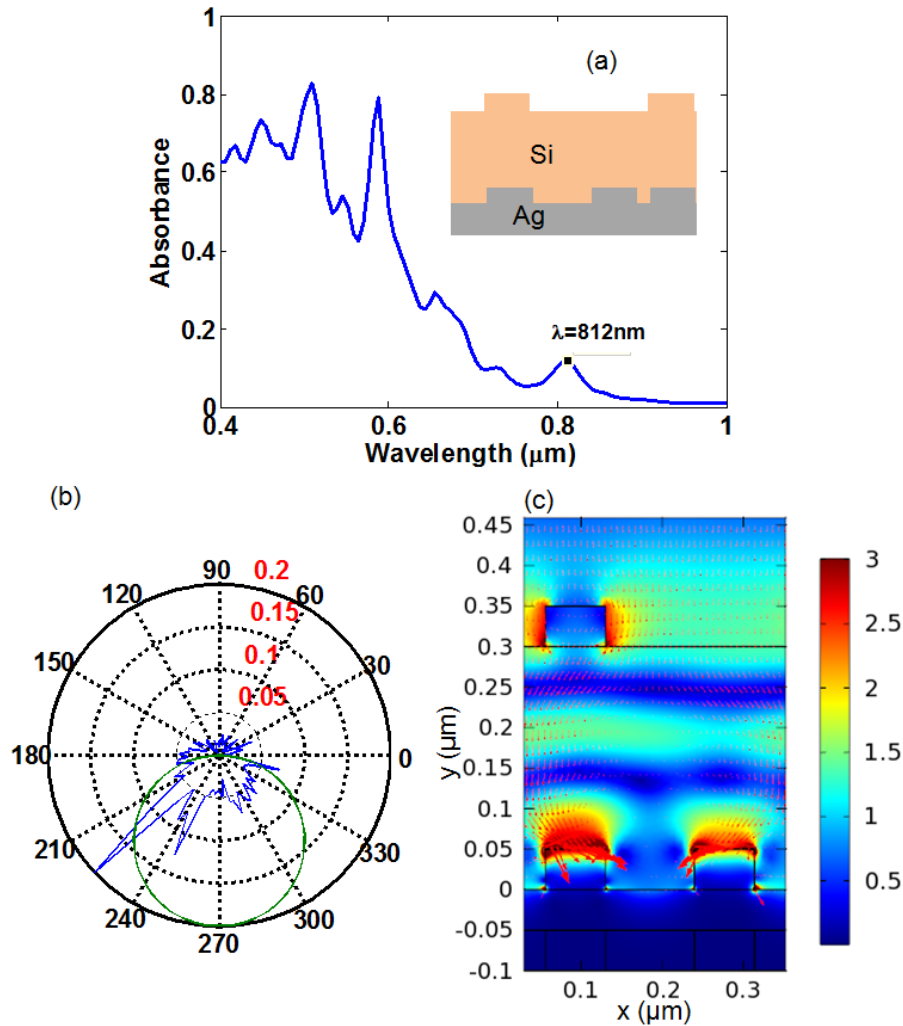


Fig. 10. (a) Spectral response, (b) angular distribution of Poynting vector, and (c) electric field profile for surface plasmon polariton (SPP) enhancement at $\lambda = 812\text{nm}$.

Figure 10 shows the spectral response, angular distribution of Poynting vector, and field profile together with Poynting vector arrow plot for surface plasmon polariton (SPP) enhancement. The only pronounced absorbance peak at long wavelength is at $\lambda = 812\text{nm}$. The long wavelength absorbance peak is used to investigate angular scattering behavior since the light trapping is essential in weak absorption regime. The averaged angle is 44.42° . SPP is observed at back reflector grating at Ag/Si interface where the field intensity exponentially decays from the interface. Here again the short wavelength absorption peak is of Fabry-Perot type so it is not chosen. The surface plasmon polariton is the coupling between surface plasmon and photon, and the result of SPP formation is the propagation along metal/dielectric interface. After solving for Helmholtz equation and matching the boundary condition of electric and magnetic field, it can be shown that the wavevector in propagation direction (x direction, parallel to the interface) and decaying direction (z direction, normal to the interface) are:

$$k_x = k'_x + ik''_x = \frac{\omega}{c} \left(\frac{\epsilon_m \epsilon_d}{\epsilon_m + \epsilon_d} \right)^{1/2} \quad (9a)$$

$$k_{z,m} = k'_{z,m} + ik''_{z,m} = \frac{\omega}{c} \left(\frac{\epsilon_m^2}{\epsilon_m + \epsilon_d} \right)^{1/2} \quad (9b)$$

In Eq. (9a) and Eq. (9b), k_x is likely to be real and $k_{z,m}$ is likely to be imaginary due to metal dielectric constant ϵ_m is negative, and this results in propagating wave parallel to the interface and evanescent wave normal to the interface. Although SPP or localized surface plasmon(LSP) type of enhancement can lead to strong localized electric field at interface, carrier interface recombination might degrade the actual photocurrent gain.

5.3 Index guided (IG) mode

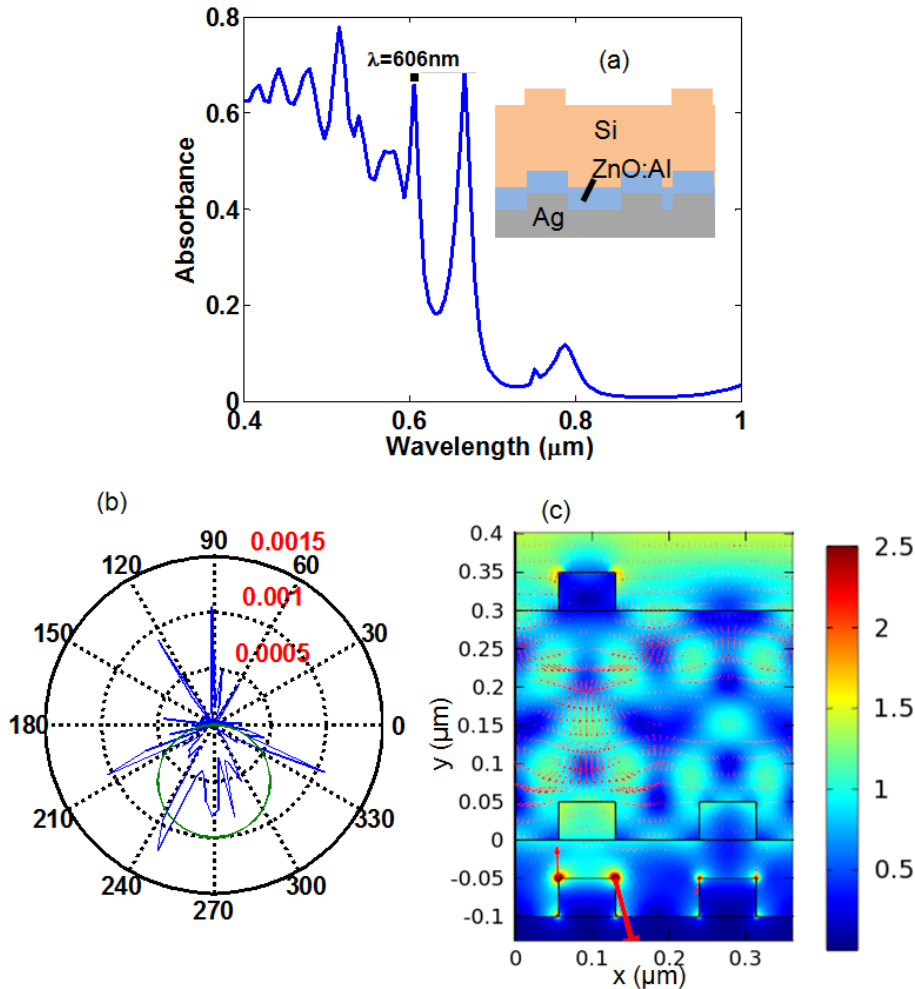


Fig. 11. (a)Spectral response, (b)angular distribution of Poynting vector, and (c) electric field profile for index-guided (IG) enhancement at $\lambda = 606\text{nm}$.

Figure 11 again shows the spectral response, angular distribution of Poynting vector, and field profile together with Poynting vector arrow plot for index-guided (IG) enhancement. The ZnO: Al spacer between Ag and silicon prevents the direct contact of metal and absorbing

silicon, and this alleviates the surface plasmon absorption loss but also reduces the chance of surface plasmon enhancement. The absorbance peak at $\lambda = 788\text{nm}$ is not chosen because it is of Fabry-Perot type resonance and exhibits very small scattering angle. The absorbance peak at $\lambda = 667\text{nm}$ is not chosen because significant surface plasmon excitation exists, despite the incorporation of dielectric spacer, at this wavelength and thus the mode coupling is a mixture of SP and IG. $\lambda = 606\text{nm}$ is chosen and waveguiding is primarily of diffractive nature. The averaged angle is 34.47° , which is significantly lower than previous SP modes for lack of large angle light scattering by SP. From the angular distribution of Poynting vector, it is seen that pronounced scattering peaks at certain angles, but in other directions the emission is much weaker. The pronounced diffraction pattern at silicon region is also observed at field profile plot, which is the explanation of pronounced scattering peak at certain angles due to the fact that the index-guided mode provides light scattering by diffraction and the peak power flow directions is where diffraction order exists. The diffraction can be conveniently expressed in terms of coupled wave analysis based on Fourier expansion:

$$\begin{aligned} & \nabla^2 E(x, z) + \omega^2 \mu \epsilon E(x, z) \\ &= \nabla^2 \left[\sum_i b_i(z) \exp(jk_{x,i} x) \right] \\ & \quad + \omega^2 \mu \epsilon \sum_i b_i(z) \exp(jk_{x,i} x) = 0 \end{aligned} \quad (10)$$

where Helmholtz equation is written in terms of different components of Fourier field, which are the diffractions in different directions. E is electric field, ϵ and μ is permittivity and permeability, ω is angular frequency b_i is Fourier coefficient of different diffraction orders and $k_{x,i}$ is the corresponding x-component of Fourier wavevector.

Here smaller Poynting vector value at angular distribution plot results from the fact that the chosen absorption peak for IG configuration is at shorter wavelength, and higher absorption coefficient leads to smaller power flow value especially deeper into the film. The exact value of Poynting vector is nonetheless not of much importance here since the relative intensity among different angles is of more interest.

6. Metallic absorption loss and interface recombination

Table 1. Comparison of Silicon Absorbance and Metallic Loss for Various Schemes

	Only bottom Ag grating in Si (no back reflector)	Only top Ag grating (no back reflector)	Planar Si slab	ETDNP	SPP	IG
Integrated Silicon Absorbance	0.2006	0.1558	0.1461	0.2147	0.2859	0.2691
Integrated Metal Absorbance	0.2153	0.0546	0	0.2492	0.2807	0.1568

The silicon absorbance and metallic absorbance for various schemes are included in Table 1. For only top Ag grating structure, no embedded bottom Ag grating in Si, and the particle height and FF of top Ag grating is optimized w.r.t. silicon integrated absorbance. For only bottom Ag grating in Si, no top Ag grating on the top of Si surface, and the geometry of embedded bottom Ag in Si is the same as ETDNP. The integrated metal absorbance for SPP is 0.2807, and adding dielectric spacer(IG) reduces it to 0.1568. This means 28.07%(or 15.68%) of solar photon, in unit of $\#\text{cm}^{-2}\text{s}^{-1}$, will be absorbed by metal. Since SPP and IG structure here is quite typical (Si/Ag or Si/ZnO/Ag), this amount of metallic loss is common in these conventional thin-film solar cell. Interested reader can repeat the calculation to verify result. Currently very few literature reports integrated metallic loss and mostly found is absorption cross-section along Mie scattering. For ETDNP, metallic loss is 0.2492, slightly lower than SPP. Although 15%-30% metal absorbance looks like high value, metallic

absorption is primarily at long wavelength where silicon absorption is weak and photon can reach metal. Thus these long wavelength photons, absorbed by metal, are unlikely to be absorbed by silicon even in the absence of metal, while SP effect enhances Si absorption at long wavelength. This is evident from the fact that IG has significantly lower metal absorption but its silicon absorption also lower than SPP (26.91% for IG and 28.59% for SPP). The metallic loss for only Ag grating on top of silicon without back reflector is much lower, but in reality back reflector is necessary, possibly with the exception of organic semiconductor where absorption is high. When back reflector is added the loss will be the same. The potential reduction for metallic absorption can be wrapping Ag with dielectric [20] to have balance between SP scattering and metal absorption, or using new metal materials to reduce metallic absorption loss such as titanium nitride [33]. It is also worth to point out the back reflector consideration for future ETDNP structure. Since the current ETDNP structure is no back reflector to isolate the effect of energy transfer, adding a back reflector and optimizing full structure will further increase efficiency. Since the surface plasmon effect has been realized in energy transfer arrays, the back reflector can be non-plasmonic structure where the metal absorption can be lower or eliminated. Dielectric mirror such as composite distributed Bragg reflector [34] or high index contrast(HCG) grating can be potential candidates. The metallic nano-particle size in Si can be reduced when back reflector is added due to the light trapping is now not only by energy transfer but also by conventional waveguiding due to air/Si/metal stack. Therefore, the metallic loss for ETDNP can be further reduced.

By using *p-i-n* diode, which is common in thin-film silicon solar cell, strong built-in electric field in intrinsic region where SP nano-particles are embedded, ensures charge collection and eliminates interfacial recombination loss. Carriers are swept out of depleted *i* region by electric field before recombination. Surface passivation is also important to reduce recombination loss in ETDNP structure. Placing metallic nano-particles in junction has been employed in organic solar cell such as organic bulk-heterojunction or tandem cell [35], and thus the proposed ETDNP can be applied well to organic photovoltaics. For plasmonic material selection, Ag provides strongest SP effect at visible range compared to Au, Cu, Al. New plasmonic material such titanium nitride or zirconium nitride provide smaller real permittivity and the tunability of dielectric response and thus is very promising to be employed in ETDNP structure to lead to lower metallic absorption loss.

7. Conclusion

Genetic algorithm and global optimization is demonstrated here to be highly effective for SP energy transfer type photovoltaic cell optimization. Result shows the avoidance of Wood-Rayleigh anomaly and excitation of SP mode with energy coupling between top/bottom and adjacent Ag nano-particles. This enables guiding the photon flow inside photovoltaic thin-film using lumped-element transmission line like structures, which provides more design versatility, compared to conventional index-guided mode or SPP back reflector. The mode coupling also increases in-plane Bloch wavevector component and leads to longer photon path length and higher solar cell absorbance. Specifically compared to SPP, LSP, or IG enhancement, Energy Transfer between Discrete Nano-Particles(ETDNP) methodology provides larger scattering angle, evident from the angular distribution of Poynting vector in silicon thin-film. Based on this work, photonic design for solar cell using successive mode coupling between surface plasmonic nano-particles is made possible, which is a new way to achieve proper control of light flow inside photovoltaic thin-film.